Inorganic Chemistry

Article

pubs.acs.org/IC

Crystal Structure and Magnetic Properties of Two New Antiferromagnetic Spin Dimer Compounds; $FeTe_3O_7X$ (X = Cl, Br)

Dong Zhang,[†,‡] Reinhard K. Kremer,[§] Peter Lemmens,[⊥] Kwang-Yong Choi,[∥] Jia Liu,[⊗] Myung-Hwan Whangbo,[⊗] Helmuth Berger,[○] Yurii Skourski,[#] and Mats Johnsson*[,†]

[†]Department of Materials and Environmental Chemistry, Stockholm University, SE-106 91 Stockholm, Sweden

[‡]College of Physics/State Key Laboratory of Superhard Materials, Jilin University, Changchun 130012, People's Republic of China

[§]Max Planck Institute for Solid State Research, Heisenbergstrasse 1, D-70569 Stuttgart, Germany

[⊥]Institute for Condensed Matter Physics, TU Braunschweig, D-38106 Braunschweig, Germany

[∥]Department of Physics, Chung-Ang University, Seoul 156-756, Republic of Korea

[⊗]Department of Chemistry, North Carolina State University, Raleigh, North Carolina 27695-8204, United States

[○]Institute of Condensed Matter Physics, Ecole Polytechnique Fédérale de Lausanne (EPFL), CH-1015, Lausanne, Switzerland

[#]Dresden High Magnetic Field Laboratory, Forschungszentrum Dresden-Rossendorf, 01314 Dresden, Germany

Supporting Information

ABSTRACT: Two new isostructural layered oxohalides $FeTe_3O_7X$ (X = Cl, Br) were synthesized by chemical vapor transport reactions, and their crystal structures and magnetic properties were characterized by single-crystal X-ray diffraction, Raman spectroscopy, magnetic susceptibility and magnetization measurements, and also by density functional theory (DFT) calculations of the electronic structure and the spin exchange parameters. $FeTe_3O_7X$ crystallizes in the monoclinic space group $P2_1/c$ with the unit cell parameters a = 10.7938(5), b = 7.3586(4), c = 10.8714(6) Å, β = 111.041(5)°, Z = 4 for $FeTe_3O_7Cl$, and a = 11.0339(10), b = 7.3643(10), c = 10.8892(10) Å, β = 109.598(10)°, Z = 4 for $FeTe_3O_7Br$. Each compound has one unique Fe^{3+} ion coordinating a distorted $[FeO_5]$ trigonal bipyramid. Two such groups share edges to form $[Fe_2O_8]$ dimers that are isolated from each other by Te^{4+} ions. The high-temperature magnetic properties of the compounds as well as spectroscopic investigations are consistent with an isolated antiferromagnetic spin dimer model with almost similar spin gaps of ~35 K for X = Cl and Br, respectively. However, deviations at low temperatures in the magnetic susceptibility and the magnetization data indicate that the dimers couple via an interdimer coupling. This interpretation is also supported by DFT calculations which indicate an interdimer exchange which amounts to 25% and 10% of the intradimer exchange for X = Cl and Br, respectively. The magnetic properties support the counterion character and a weak integration of halide ions into the covalent network similar to that in many other oxohalides.

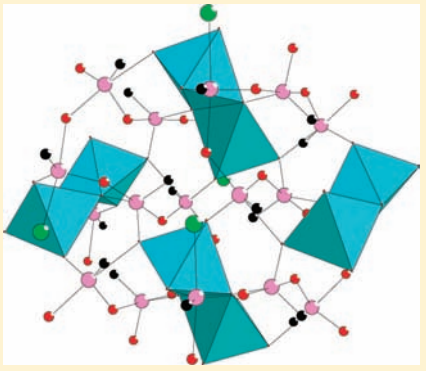

1. INTRODUCTION

Oxohalides comprising transition metal cations and p-element cations with stereochemically active lone-pairs constitute a group of compounds with rich crystal chemistry. The search for novel phases lead to several structurally low-dimensional compounds and even quantum spin systems with interesting magnetic properties.[1−6] The lone-pair electrons occupying a nonbonding orbital are stereochemically active and can be regarded as an additional ligand that allows for asymmetric or one-sided coordination around the lone-pair cation. The role of lone pair distortions in structural chemistry has been addressed in several studies.[7−14]

The aim of this work is to search for new low-dimensional compounds in the Fe^{3+}-Te^{4+}-O-X (X = Cl, Br) system and characterize their magnetic properties. Previously described compounds in this family include $FeTe_2O_5X$,[3] $Fe_5(TeO_3)_6Cl_2$,[15] $Fe_4Te_6O_{16}X_3$,[15] and $Fe_3(TeO_3)_3OCl$.[16] The relatively strong Lewis acids Fe^{3+} and Te^{4+} preferably form bonds with oxygen in an oxochloride or an oxobromide such that the halide ions become expelled from the covalently bonded oxide network and act more as counteranions. Our synthetic effort led to two new compounds, $FeTe_3O_7Cl$ and $FeTe_3O_7Br$, whose structural and magnetic properties are characterized in the following.

2. EXPERIMENTAL SECTION

Single-crystals of yellow-green $FeTe_3O_7Cl$ (**1**) and dark orange/brown $FeTe_3O_7Br$ (**2**) have been grown by a standard chemical vapor phase method. The crystals were prepared from a mixture of analytical grade

Received: September 26, 2011
Published: November 11, 2011

Fe_2O_3, TeO_2, and FeX_3 (X = Cl, Br) from the nonstoichiometric molar ratio 1:6:1 and the stoichiometric ratio 1:9:1. The starting powder mixtures were sealed in quartz tubes with electronic grade HCl or HBr as transport gas for the crystal growth. The ampules were placed horizontally in a tubular two-zone furnace and heated at a rate of 50 °C/h to 500 °C and kept there for six weeks. The optimum temperatures at the source and deposition zones for the growth of single crystals were 500 and 440 °C, respectively. The main product from the synthesis experiments was $FeTe_2O_5X$ and only minor amounts of $FeTe_3O_7X$ were formed. The maximum $FeTe_3O_7X$ crystal size was 8 × 10 × 1 mm^3.

Single-crystal X-ray diffraction data were collected on an Oxford Diffraction Xcalibur3 diffractometer system using graphite-monochromatized MoKα radiation, λ = 0.71073 Å. The intensities of the Bragg reflections were integrated using the software CrysAlis RED with analytical absorption correction.[17] The structure was solved by Direct Methods, using the SHELXTL crystallographic software package.[18] The structural drawings were made with the program DIAMOND.[19] The crystal data for the two phases are summarized in Table 1.

Table 1. Crystal Data and Structure Refinement Parameters for $FeTe_3O_7Cl$ and $FeTe_3O_7Br$

empirical formula	$FeTe_3O_7Cl$ (**1**)	$FeTe_3O_7Br$ (**2**)
formula weight	586.10	630.56
temperature (K)	293(2)	293(2)
wavelength (Å)	0.71073	0.71073
crystal system	monoclinic	monoclinic
space group	$P2_1/c$	$P2_1/c$
a (Å)	10.7938(5)	11.03390(10)
b (Å)	7.3586(4)	7.36430(10)
c (Å)	10.8714(6)	10.88920(10)
β (deg)	111.041(5)	109.5980(10)
volume (Å^3)	805.91(7)	833.564(16)
Z	4	4
density$_{calc}$, (g cm^{-3})	4.831	5.025
absorption coefficient (mm^{-1})	12.843	16.890
F(000)	1020	1092
crystal color	green	brown
crystal habit	block	block
crystal size	0.1118 × 0.1055 × 0.0309	0.1149 × 0.0978 × 0.0587
θ range for data collection (deg)	4.33 to 26.35	4.25 to 26.37
index ranges	$-13 \le h \le 13$	$-13 \le h \le 13$
	$-8 \le k \le 9$	$-9 \le k \le 9$
	$-13 \le l \le 13$	$-13 \le l \le 13$
reflections collected	9874	10222
independent reflections	1635 [R(int) = 0.0227]	1648 [R(int) = 0.0240]
data/restraints/parameters	1635/0/110	1648/0/110
goodness-of-fit on F^2	1.002	1.005
final R indices [$I > 2\sigma(I)$][a]	R_1 = 0.0151	R_1 = 0.0244
	wR_2 = 0.0377	wR_2 = 0.0678
R indices (all data)	R_1 = 0.0181	R_1 = 0.0263
	wR_2 = 0.0389	wR_2 = 0.0690

[a] $R_1 \sum||F_o| - |F_c||/\sum|F_o|$; $wR_2 = \{\sum[w(F_o^2 - F_c^2)^2]/\sum[w(F_o^2)^2]\}^{1/2}$.

The magnetic susceptibilities of thin platelet-shaped crystals of **1** and **2** were measured with a MPMS-XL SQUID magnetometer (Quantum Design) at temperatures between 2 and 400 K and in fields up to 7 T. The crystals were mounted with a minute amount of a fast drying varnish with the field in the (011) plane of the platelets.

Magnetization measurements were performed at the Dresden High Magnetic Field Laboratory using a pulsed field magnet with fields up to 60 T. The 20 ms-duration pulsed field was applied along the c-axis of a single crystal. The magnetic moment was detected by an induction method with a pick-up coil device at the lowest available temperature of 1.4 K.

Raman scattering experiments were performed using a laser (λ = 532.1 nm, P = 3 mW) in backscattering configuration. The single crystalline samples were kept in a variable temperature closed cycle cryostat (Optistat, T = 2.8−300 K).

The spin exchange interactions of **1** and **2** were evaluated on the basis of density functional theory (DFT) calculations. Our calculations employed the frozen-core projector augmented wave (PAW) method encoded in the Vienna ab initio simulation packages (VASP),[20] and the generalized-gradient approximation (GGA)[21] with the plane-wave-cutoff energy of 500 eV and a set of 9 and 24 k-points for the irreducible Brillouin zone for the calculations of density of state (DOS) and spin exchange interaction constants.

3. RESULTS AND DISCUSSION

3.1. Crystal Structure. The two new isostructural compounds **1** and **2** crystallize in the monoclinic system, space group $P2_1/c$, with the unit cell parameters given in Table 1. The crystal structure is made up of covalently bonded Fe−Te−O slabs, and the halide ions are located in between them so that only weak van der Waals interactions are present between adjacent slabs. A projection view along the b-axes is shown in Figure 1a. Bond valence sum (BVS) calculations[22,23] resulted in

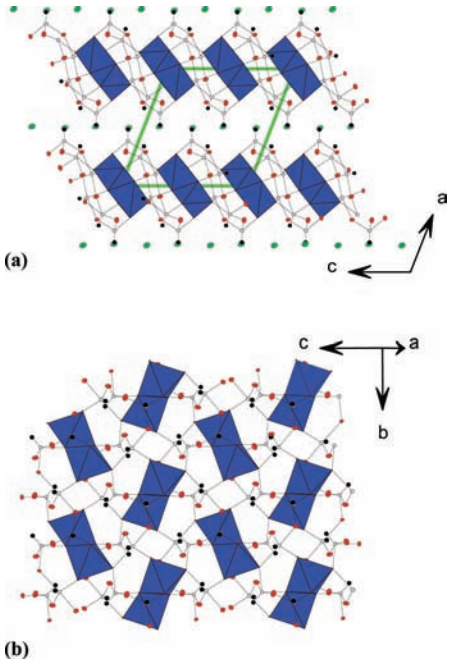

Figure 1. (**a**) Overview of the layered crystal structure for $FeTe_3O_7X$ (X = Cl, Br) along [010]. (**b**) An oxide slab showing how the [Fe_2O_8] groups (blue polyhedra) are isolated from each other by Te atoms (gray). O is red, the lone pair on Te^{4+} is marked as a black circle.

values between 4.0 and 4.2 for the Te^{4+} and near 3.0 for the Fe^{3+} cations. The halide ions, however, indicated lower than expected values as will be discussed below.

There is one crystallographically unique Fe^{3+} cation forming a distorted [FeO_5] trigonal bipyramid with average Fe−O distances of 1.949(3) Å in **1** and 1.952(4) Å in **2**, respectively. Two such trigonal bipyramids have a common edge to form [Fe_2O_8] dimer units, see Figure 2a,b. The Fe−Fe distance within such a dimer is 3.236(7) Å in **1** and 3.232(2) Å in **2**,

dx.doi.org/10.1021/ic202093s | Inorg. Chem. 2011, 50, 12877−12885

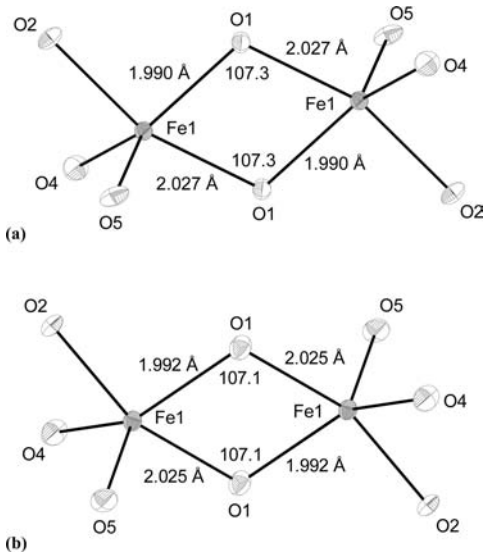

Figure 2. $[Fe_2O_8]$ groups in the two compounds (**a**) $FeTe_3O_7Cl$ (**1**) and (**b**) $FeTe_3O_7Br$ (**2**).

respectively. The dimers are isolated from each other by Te^{4+}-cations (Figure 1b), and the closest Fe–Fe distance in between two dimers in the same oxide slab is 5.711(1) Å in **1** and 5.724(1) Å in **2**.

The three crystallographically different Te^{4+} cations can all be described as having asymmetric one-sided Te–O coordinations. Each Te(1) bonds to four oxygen atoms forming a $[Te(1)O_4]$ seesaw with Te–O bonding distances in the range 1.894(2)–2.119(2) Å. Each Te(2) coordinates four oxygen atoms with three shorter distances in the range 1.867(3)–1.951(3) Å and one longer at 2.426(3) Å, which results in a $Te(2)O_{3+1}$ seesaw. Each Te(3) bonds to three oxygen atoms forming a $[Te(3)O_3]$ trigonal pyramid with bonding distances in the range 1.867(3)–1.916(3) Å. The distances given above are for compound **1**, and very similar values are also found for **2**. There is only one unique halogen atom in the two isostructural compounds, and the Te···Cl distances are in the range 3.049(1)–3.252(4) Å, and the Te···Br distances in the range 3.174(1)–3.301(1) Å. These Te···X (X = Cl, Br) distances are too long to be considered as belonging to the primary bonding sphere of the Te atom. However, the Te···X contacts preserve the structural integrity. If these Te···X contacts are taken into consideration, the coordination environments around Te(2) and Te(3) are described as $[Te(2)O_4X]$ and $[Te(3)O_3X_3]$, respectively. For Te(1) the closest halide ion, however, is as far away as 4.622(5) Å in **1** and 4.770(1) Å in **2**. BVS calculations for the halide ions give values of 0.52 for Cl in **1** and 0.60 for Br in **2** if we include the Te···X contacts up to 3.4 Å. Thus, the halide ions cannot be considered as fully integrated into the covalent network but instead act more as counteranions as found also in other oxohalides such as $Fe_5(TeO_3)_6Cl_2$ and $Fe_3(TeO_3)_3OCl$.[15,16] The Te coordination polyhedra polymerize to form $[Te_3O_9]_\infty$ ladders running along [010], see Figure 3. The ladders are connected in the [001] direction to the $[Fe_2O_8]$ dimer units via common oxygens to form covalently bonded $[FeTe_3O_7]_\infty^{+1}$ oxide slabs, which are separated by halide ions, see Figures 1a-b. The lone-pairs on the Te^{4+} cations protrude toward the nonbonding regions in the crystal structure, that is, from the oxide slabs to available space in between the halide ions.

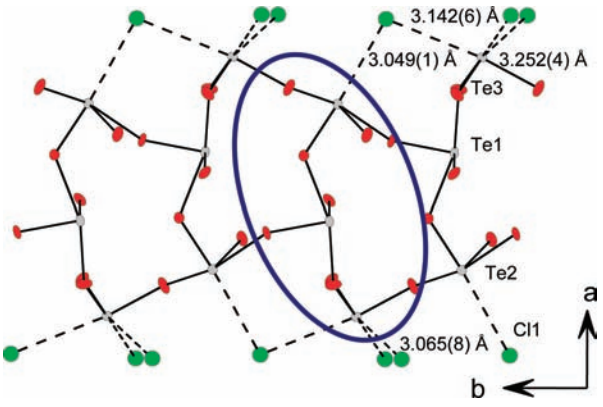

Figure 3. $[Te_3O_9]_\infty$ ladders that extend along [010] in $FeTe_3O_7Cl$, Te–Cl distances up to 3.3 Å are marked. The blue circle marks one $[Te_3O_9]$ group.

The previously characterized compounds of the Fe–Te–O–X (X = Cl, Br) systems are mainly of two types; (*i*) layered structures that have weak van der Waals interactions in between the layers, for example, $FeTe_2O_5X$[3] and **1** and **2**. (*ii*) Three dimensional framework structures where the halide ions are located in channels of the crystal structure, for example, $Fe_5(TeO_3)_6Cl_2$[15] and $Fe_3(TeO_3)_3OCl$.[16] The compound $Fe_4Te_6O_{16}X_3$[15] shows resemblances with both types and consists of layers but does also contain channels where the halide ions are located.

3.2. Low-Field Magnetic Susceptibility of Single Crystals. The magnetic susceptibilities of **1** and **2** are field independent and their temperature dependence is very similar, see Figure 4. The susceptibilities are characterized by a broad

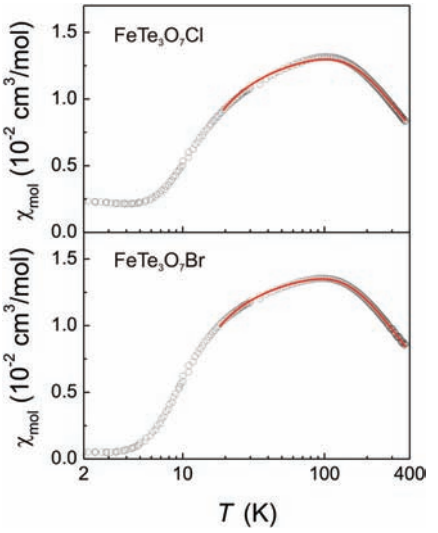

Figure 4. Magnetic susceptibilities measured with a field of 0.1 T applied within the platelet planes of crystals of $FeTe_3O_7X$ (X = Cl, Br). The solid (red) lines are fits to the susceptibility of a dimer unit of Fe^{3+} ($S = 5/2$) cations with parameters listed in Table 2.

maximum at ~102 K for **1** and ~94 K for **2**, a Curie–Weiss behavior above these temperatures, and a very steep decrease below the maximum. At very low temperatures the susceptibilities level off at values of $\sim 2 \times 10^{-3}$ cm^3/mol for **1** and $\sim 6 \times 10^{-4}$ cm^3/mol for **2**.

dx.doi.org/10.1021/ic202093s | Inorg. Chem. 2011, 50, 12877–12885

Table 2. Fitted *g*-Factors, Spin-Exchange Parameters *J*, Impurity Fraction *y*, and Structural Parameters Related to the Fe−O−Fe Bonding in a Dinuclear Unit[a]

X	*g*	*J* (K)	χ_0 (10^{-6} cm^3/mol)	$y \times 10^4$	*d*(Fe−O) (Å)	∠Fe−O−Fe (deg)
Cl	1.999(5)	−35.4(2)	−162	∼0	1.9897(32)	107.21(13)
					2.0286(21)	
Br	1.992(1)	−34.0(5)	−172	0.0024(3)	1.9918(45)	107.14(19)
					2.0251(40)	

[a]The temperature independent term χ_0 was fixed to the value obtained by summing the diamagnetic increments for the respective cations as tabulated by Selwood.[25] Inclusion of a Curie-Weiss temperature into the impurity susceptibility was not found necessary.

The magnetic susceptibilities were fitted to an expression comprising the spin susceptibility of an isolated spin dimer $\chi_{spin}(T)$, a temperature independent term χ_0 accounting for the diamagnetic susceptibilities of the closed shells and possible van Vleck paramagnetic contributions, and a Curie- type susceptibility $\chi_{imp}(T)$ introduced to take care of impurities or lattice imperfections generating magnetic single ion defects. The susceptibility of free ion impurity contributions tends to diverge at low temperatures, but this was not apparent experimentally. Thus the impurity contributions are very small but not negligible since the spin susceptibility of the dimer unit should vanish exponentially toward $T \rightarrow 0$.

$$\chi(T) = (1 - y)\chi_{spin}(T) + \chi_0 + y\chi_{imp}(T) \quad (1)$$

with

$$\chi_{imp}(T) = \frac{C}{T} \quad (2)$$

where C is the Curie constant, $C = N_A g^2 \mu_B^2 S(S + 1)/3k_B$ with $S = 5/2$, and y the fraction of the total number of spin entities that are not coupled in a spin dimer unit.

Starting with a Hamiltonian for a spin dimer and assuming Heisenberg isotropic spin exchange interaction between the spin entities $\vec{S}_i$ ($i = 1, 2$)

$$H = -J\vec{S}_1 \cdot \vec{S}_2 \quad (3)$$

one obtains the spin susceptibility $\chi_{spin}(T)$ of a spin dimer system following the van Vleck expansion (i.e., one remains in the limit $B \rightarrow 0$) per one spin center[24]

$$\chi_{spin}(T) = \frac{\mu_0 N_A g^2 \mu_B^2}{k_B T} \times \frac{e^x + 5e^{3x} + 14e^{6x} + 30e^{10x} + 55e^{15x}}{1 + 3e^x + 5e^{3x} + 7e^{6x} + 9e^{10x} + 11e^{15x}} \quad (4)$$

where N_A is Avogadro's number, μ_B the Bohr magneton, k_B the Boltzmann constant, g the g-factor that may be safely assumed to be very close to the free electron value for the half-filled spin only system Fe^{3+} (d^5, $S = 5/2$). For the temperature independent part χ_0, we used the sum of the diamagnetic susceptibilities of the constituent ions tabulated by Selwood to find $\chi_0 = -162 \times 10^{-6}$ cm^3/mol for **1** and -172×10^{-6} cm^3/mol for **2**. Table 2 summarizes the parameters obtained from the fits of eq 1 to the experimental data between 20 K and ∼380 K measured with an external field of 0.1 T. Additionally, also some structural parameters concerning the Fe spin dimer unit have been listed. The high temperature data fit very well to eq 4 using a single exchange parameter. Below 20 K deviations appear which indicate the need of corrections to the simplified dimer model with only a single exchange parameter.

Other contributions to the susceptibility, for example, the magnetization of broken dimers or other imperfections in the crystal which lead to a single-ion contribution may also be considered. However, their contribution to the magnetization are expected to diverge, adverse to the experimental observations.

DFT calculations (see below) rather indicate appreciable interdimer exchange interaction between 10 and 20% of the intradimer exchange (Table 3). Interchain interaction will lead to a dispersion of the excited dimer states and an extension of the dimer model. In the following we describe low-temperature high-field magnetization measurements which indeed reveal deviations from the dimer magnetization which can be modeled by assuming a dispersion of the excited dimer states.

Table 3. Spin Exchange Constants J_1, J_2, and J_3 (in meV) for $FeTe_3O_7Cl$ and $FeTe_3O_7Cl$ Obtained from GGA Calculations

	J_1	J_2	J_3
$FeTe_3O_7Cl$	−6.54	+1.62	−0.83
$FeTe_3O_7Br$	−6.55	+0.62	−0.80

3.3. High-Field Magnetization. High field magnetization measurement on **2** carried out at 1.4 K is shown in Figure 5.

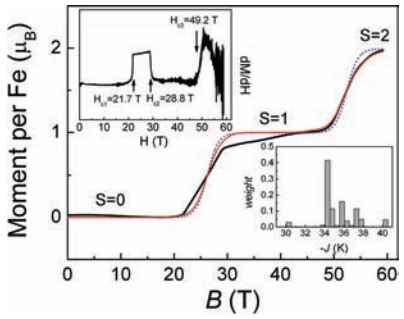

Figure 5. Magnetization and derivative of the magnetization with respect to the field (upper inset) of $FeTe_3O_7Br$ measured in a pulsed field at 1.4 K. The (black) solid line represents the experimental data, the (blue) dashed line is a fit according to eqs 5 and 7 assuming a (single) dimer exchange parameter of −35.3K and a temperature of 1.4 K. The (red) solid line represents the best fit which is obtained by using a distribution of exchange parameters around 35.3 K with weights as displayed in the lower inset.

Two equally spaced steps are centered at about 26 and 52 T. At each step the magnetization jumps by 1 μ_B/Fe atom. The width of the step is about 7 T as can be seen from the derivative of the magnetization with respect to the field shown in the inset. To model the field dependence of the magnetization, we express the energy of a spin dimer under magnetic field as the spin

dx.doi.org/10.1021/ic202093s | Inorg. Chem. 2011, 50, 12877–12885

dimer energy described by the Hamiltonian eq 3 plus the Zeeman energy, namely,

$$E(S^T, S_1, S_2) = -\frac{J}{2}[S^T(S^T+1) - S_1(S_1+1) - S_2(S_2+1)] + \mu_B g m_{S^T} B \quad (5)$$

Where the total spin S^T represents the sum of the two spins in the spin dimer unit,

$$\vec{S}^T = \vec{S}_1 + \vec{S}_2 \quad (6)$$

and the magnetic quantum number m_{S^T} of the total spin S^T varies between $-S^T$, $-S^T+1$, ...,S^T-1, S^T. The energy eigenvalues according to eq 5 are subsequently used to calculate the magnetization per Fe atom according to eq 7

$$M = -\frac{\sum_n \partial E_n(S^T)/\partial B \exp(-E_n(S^T)/k_B T)}{\sum_n \exp(-E_n(S^T)/k_B T)} \quad (7)$$

In the fits we varied the spin exchange parameter J using a temperature of 1.4 K as fixed experimentally. The fit reproduces well the magnetization steps with a spin exchange parameter of $J = -35.3(1)$ K for **2** in agreement with the spin exchange value obtained from the susceptibility fit. However, the magnetization steps are considerably more smeared than the calculations predict and, additionally, above the first step the magnetization exhibits a linearly increasing part before it reaches the plateau value of 1 μ_B/Fe atom. As a consequence of the broadened transition instead of a rounded shape, as expected for a thermally activated behavior, the derivative dM/dB of the magnetization with respect to the magnetic field exhibits an almost rectangular shape with a width of ~7 T (inset in Figure 5).

We ascribe these deviations to interdimer exchange interactions and some dispersion of the excited states. To model these deviations we fitted the magnetization of **2** by allowing a discrete distribution of the dimer exchange centered about the exchange parameter (35.3 K) obtained from the fit of a simple dimer model described above. We subsequently fitted the magnetization data by varying the weights of 21 discrete exchange parameters in the interval 30.3 K $\leq J \leq$ 40.3 K and obtained a markedly improved fit. Especially, the step-like increase to the second plateau above 45 T is reproduced significantly better. The fitted weights (average of 9 independent runs) suggest a distinct separation of the exchange energies in three equidistant peaks between −34 and −38 K with a weight ratio of ~3:1:1. The dominant peak is found at an energy −34 K which is in good agreement with the exchange value obtained from the fit of the high temperature susceptibility data. The overall energy splitting of the peak spectrum amounts to about ~10% of the energy of the dimer exchange constant which is close to the ratio of the intradimer to interdimer exchange values obtained from the DFT calculations (see Table 3).

Averaging over all energies with the appropriate weights, w_i, we find that the mean value of the exchange values, $\sum_{i=1}^{21} w_i J_i$, is preserved. It amounts to 35.4 K, very close to the exchange parameter obtained by fitting a simple dimer model to the magnetization. These results provide further evidence that **1** and **2** essentially represent spin-dimer systems, however, with noticeable interdimer coupling. There still exist deviations in the field regime of the first plateau mainly because the magnetization slightly increases above 30 T. Since the magnetization below 20 T is totally flat, a finite slope of the magnetization at the first plateau is not expected. Thus, this effect is not due to anisotropic interactions, which are not included in our simulation. Rather, it should be attributed to an instrumental artifact related to the pulsed field experiment.

3.4. Raman Scattering. Raman scattering measurements probe both phonons and magnetic modes[26] and can shed light on possible instabilities of the compound as well as on their respective energy scales.[27] Furthermore, the coupling of lattice and spin degrees of freedom via spin orbit coupling may induce phonon anomalies.[28] In general, lone pair compounds show a strong enhancement of the Raman scattering cross section. This is due to the high electronic polarizability of their electronic states. The existing Raman studies on related lone pair compound[3,4,16,29] can be used as the reference for the effects discussed below.

Figure 6 shows Raman spectra for **1** and **2**, at T = 3 K in the (aa) and (bb) polarization, that is, with the incident and

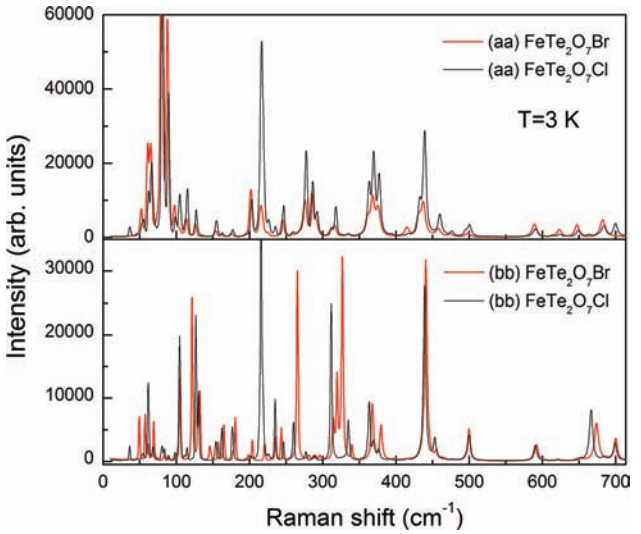

Figure 6. Raman spectra for $FeTe_3O_7Cl$ and $FeTe_3O_7Br$ at T = 3 K in (aa) and (bb) polarization, in the upper and lower panels, respectively.

scattered light polarization both parallel and within the *ab* plane. In Figure 7 we compare the (cc) and (bc) polarization for **2** at two different temperatures. We observe a large number of partially overlapping modes that are attributed to phonon excitations. These modes group into three regimes according to their frequency and approximate separation. We attribute this grouping to the specific atomic coordination environments. The modes 40−180, 200−500, 550−850 cm^{-1}, correspond to the vibrational modes of the heavy atomic coordinations, light groups, and halides, based on literature and earlier Raman scattering studies.[30]

The highest and lowest frequencies of the phonon modes, 42 and 850 cm^{-1}, are reasonable for the wide range of different atomic masses and binding potentials realized in $FeTe_3O_7X$. The spectra of **1** and **2** are very similar in energy distribution, mode line-width, and anisotropy of the scattering intensity. This is attributed to the weakly bonded halide ions that act more as counterions and only contribute to a few normal modes. In the following, we will focus on **2**.

A symmetry analysis of the monoclinic space group, $P2_1/c$, shows that each atom occupies a Wyckoff position 4e and thereby contributes to Raman scattering with $3A_g$ and $3B_g$

dx.doi.org/10.1021/ic202093s | Inorg. Chem. 2011, 50, 12877−12885

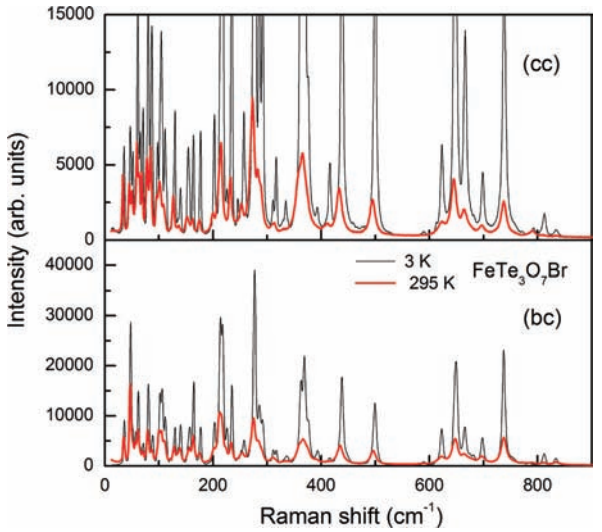

Figure 7. Effect of temperature on Raman spectra of $FeTe_3O_7Br$ with (cc) and (bc) polarization. In these light polarizations also the grouping of the modes into three frequency regimes is evident.

modes.[31] In infrared absorption this site contributes $3A_u$ and $3B_u$ modes, each. The A_g symmetry modes may be observed with any light polarization in the (110) plane and parallel light polarization along the crystallographic (001) plane. The B_g modes may be observed with the remaining polarizations having one (incident or scattered) light polarization parallel to the *c*-axis. This leads to a sum of Γ_{Raman}= 36 A_g and 36 B_g Raman active modes. For the Raman spectra of **1** and **2** we count a sum of 69 and 70 partially overlapping modes. This number is very reasonable, given the low symmetry of the atomic positions and the large variation of the scattering intensities.

As a function of temperature all phonon modes show a strongly enhanced scattering intensity and a moderate, anharmonic hardening of frequency. The increasing scattering intensity could point to an electronic instability or a change in the electronic states that are involved in the generation of the electron-hole pair during the Raman scattering process. The observed anharmonicity of the optical phonon modes is induced by a decay of the modes into other quasiparticles, as a pair of zone boundary phonons or magnons. These processes depend on the respective density of states and matrix elements. A detailed analysis of the frequency, line width, and intensity can shed light on these processes.

Figures 8 and 9 show frequency, line width and intensity of the modes at 165, 278, 439, and 650 cm^{-1} for **2** as a function of temperature. Because of their different energies, the given modes represent typical normal modes. The scaling of the given plots is identical allowing for a direct comparison of the effects. All modes show a very similar variation of intensity. It is evident that the intensity gain is based on the excitation process and not on the individual mode. We attribute it to the large polarizability of lone-pair electronic states in oxyhalides and their participation in the Raman scattering process.

In contrast, the phonon frequency and line-width show an individual variation with temperature. While the modes in the medium frequency range (278 and 439 cm^{-1}) exhibit a frequency hardening by approximately 3 cm^{-1} and a comparably large reduction of phonon line-width by 9 cm^{-1} on reducing the temperature, the other two modes exhibit a weaker effect (up to a factor two). We attribute this difference to a contribution of the electronic Fe states to the binding potential of the two medium frequency phonon modes. Because of spin orbit coupling, enhanced spin-phonon and

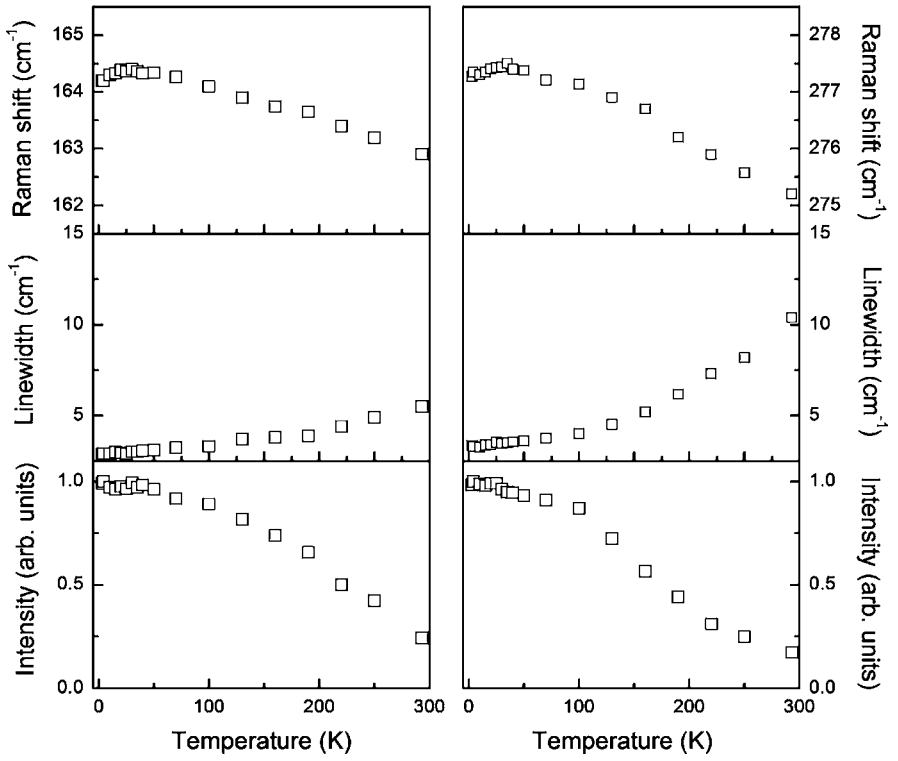

Figure 8. Properties of the phonon modes at 165 and 278 cm^{-1} as function of temperature for X = Br. The scaling of the plots is the same for each mode to allow a direct comparison.

dx.doi.org/10.1021/ic202093s | Inorg. Chem. 2011, 50, 12877–12885

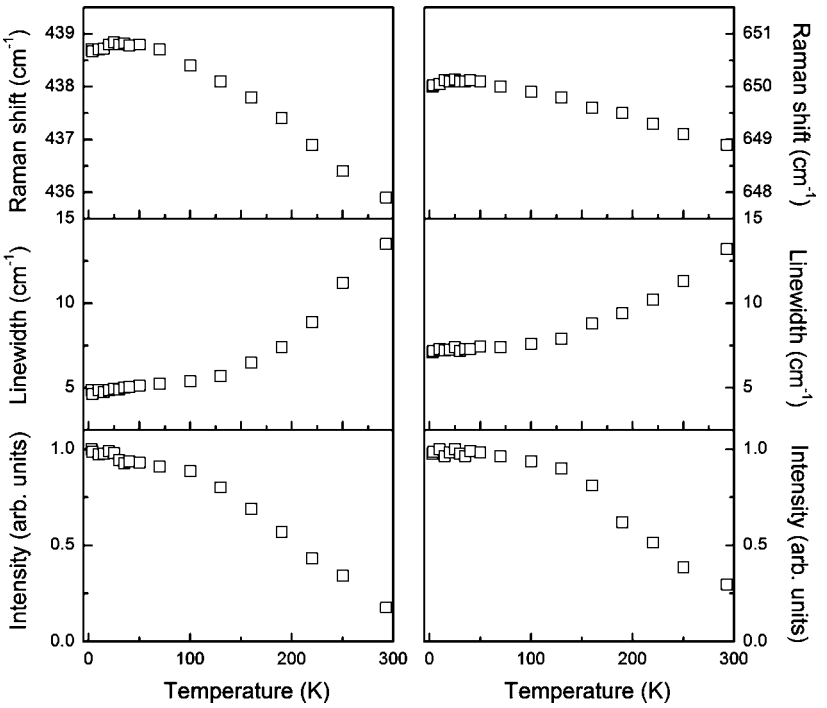

Figure 9. Properties of the phonon modes at 439 and 650 cm^{-1} as function of temperature for X = Br. The scaling of the plots is the same for each mode to allow a direct comparison.

phonon−phonon interactions may enhance anharmonicity. Further evidence for spin-phonon coupling is also found in the small softening of the phonon frequencies at temperatures below approximately 30 K, a temperature scale comparable to the dominant coupling constant of the spin system. We note that, in the pseudocubic manganites $LnMnO_3$, the rotational, Jahn−Teller, and breathing modes of the MnO_6 octahedra have similar energies (270−580 cm^{-1}) and show a pronounced temperature dependency because of their coupling to electronic degrees of freedom.[32]

We also searched for magnetic Raman scattering due to spin exchange processes. This scattering contribution is frequently observed in spin systems when more than two magnetic ions are coupled by a considerable spin exchange interaction, and is comparable in energy to the exchange coupling *J*. Magnetic Raman scattering was observed neither in **1** nor in **2**, which indicates indirectly the interpretation of the magnetic system as being dominated by a spin dimer with weaker interdimer interaction.

3.4. Evaluation of Spin Exchange Interactions. To confirm our experimental conclusion that the magnetic properties of **1** and **2** are well described by an isolated antiferromagnetic dimer model, we evaluate the spin exchange interactions of **1** and **2** by first principles DFT GGA calculations. Our spin-polarized calculations predict that **1** and **2** are magnetic insulating even without adding on-site repulsion U on Fe, as can be seen from the DOS plots calculated for the ferromagnetic state of **1** in Figure 10. Thus, we did not use DFT+U calculations[33] for our evaluations of the spin exchange interactions.

For **1** and **2** we consider three spin exchange interactions J_1−J_3 defined in Figure 11, where J_1 is the intradimer spin exchange while J_2 and J_3 are interdimer spin exchanges. To evaluate these interactions, we determine the relative energies

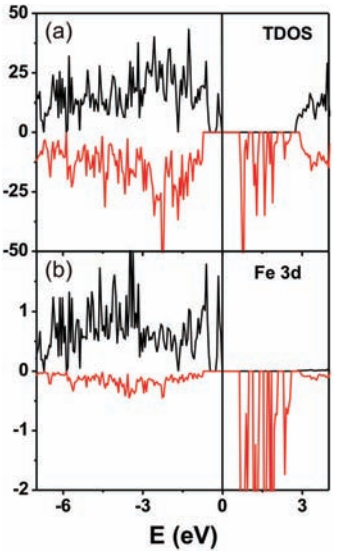

Figure 10. Spin polarized electronic density of states (states/electron FU) of $FeTe_3O_7Cl$ in the FM configuration (see Figure 12). (**a**) Total density of states. (**b**) Projected density of states of the Fe d electrons.

of the four ordered spin states, FM, AF1, AF2, and AF3, using the (a, 2b, c) supercell. The relative energies of these states calculated by performing GGA calculations are also summarized in Figure 12. To extract the values of J_1−J_3, we express the total spin exchange interaction energies of the eight ordered spin states in terms of the spin Hamiltonian, $\hat{H} = -\sum_{i<j} J_{ij} \hat{S}_i \cdot \hat{S}_j$, where $J_{ij} = J_1$−J_3 is the spin exchange constant for the interaction between the spins $\hat{S}_i$ and $\hat{S}_i$ at the sites *i* and *j*, respectively. By applying the energy expression obtained for spin dimers consisting of two spin sites with *N* unpaired spins (i.e., $N = 5$ for Fe^{3+}), the total spin exchange energies, per supercell, that is, per eight formula units (FUs), of the four

dx.doi.org/10.1021/ic202093s | Inorg. Chem. 2011, 50, 12877−12885

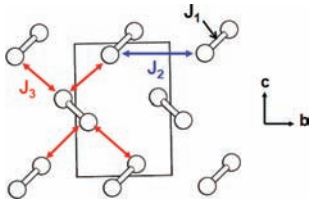

Figure 11. Definition of the three spin exchange parameters J_1 (intradimer), J_2, and J_3 (both interdimer) in $FeTe_3O_7X$ (X = Cl, Br).

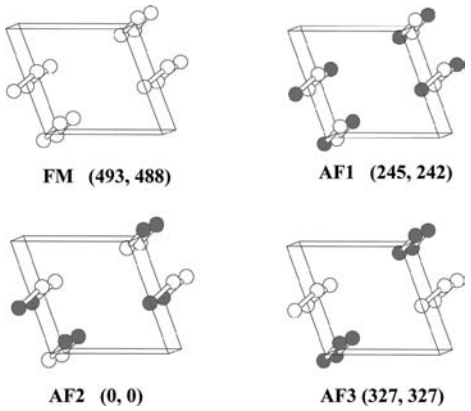

Figure 12. Four ordered spin states FM, AF1, AF2, and AF3 in a (a, 2b, c) supercell employed to extract the values of J_1, J_2, and J_3, where only the Fe atoms are shown for simplicity. The up-spin and down-spin Fe sites are represented by spheres of different colors. The numbers in parentheses give the relative energies (in meV) obtained from the GGA calculations with for **1** and **2**, respectively.

ordered spin states are written as

$$E_{FM} = (-4J_1 - 8J_2 - 16J_3)(N^2/4)$$
$$E_{AF1} = (+4J_1 + 8J_2)(N^2/4)$$
$$E_{AF2} = (+4J_1 - 8J_2 + 16J_3)(N^2/4)$$
$$E_{AF3} = (-4J_1 - 8J_2 + 16J_3)(N^2/4)$$

Then, by mapping the relative energies of the four ordered spin states determined from GGA calculations onto the corresponding relative energies determined from the above expressions, we obtain the values of J_1–J_3 listed in Table 3. The antiferromagnetic intradimer exchange J_1 dominates. The interdimer spin exchanges are weak but are not negligible. This finding supports the description of the magnetic properties of **1** and **2** in terms of an antiferromagnetic isolated dimer model. For **1** and **2**, the calculated J_1 values are essentially the same, and so are the interdimer exchange J_3. However, **1** and **2** differ mainly in the interdimer exchange J_2. We note that the calculated J_1 values are about −6.5 meV (75.4 K) and thus by a factor of 2 greater than the experimental values. This finding is in line with the general experience that GGA calculations tend to overestimate spin exchange constants, while the ratios between them are maintained.

4. CONCLUDING REMARKS

Two new iron oxohalides $FeTe_3O_7X$ (X = Cl, Br) were synthesized, and their structural and magnetic properties were characterized. In these layered compounds the oxide slabs made up of the $[Fe_2O_8]$ dimer units are linked by the $[Te_3O_9]_\infty$ sublayers. The halide ions are located in between the slabs at such long distances from the Te^{4+} ions that they cannot be considered as being a part of the covalent network. The Fe atoms are coordinated by only oxygen, as in $FeTe_2O_5X$ (X = Cl, Br)[3] and $Fe_3Te_3O_{10}Cl$.[16] In similar oxohalides with late transition metal ions such as Cu^{2+} or Ni^{2+} the metal cations tend to bond to both oxide and halide ions[2,29] while Cu^+ most often bond only to halide ions.[15,34] Thus the Lewis acidity and the softness of the metal cations have significant influence on the resulting crystal structure because of their bonding preferences. The magnetic properties of $FeTe_3O_7X$ (X = Cl, Br) are well described by an isolated antiferromagnetic spin dimer model with spin gaps of approximately ∼−35 and ∼−34 K for X = Cl and Br, respectively. The largest exchange coupling constant J_1 that forms the spin dimer is antiferromagnetic and of the same size. High-field magnetization experiments are in agreement with the low-field magnetic susceptibility data, and point to some dispersion of the higher spin multiplets leading to a smearing of the magnetization steps. These observations are supported by the spin exchange interactions of $FeTe_3O_7X$ (X = Cl, Br) obtained from GGA calculations.

■ ASSOCIATED CONTENT

Ⓢ Supporting Information

Tables of atomic coordinates and equivalent isotropic displacement parameters, bonding distances and angles, and Bond Valence Sum (BVS) calculations. This material is available free of charge via the Internet at http://pubs.acs.org. Further details on the crystal structural investigations can be obtained from the Fachinformationszentrum Karlsruhe, Abt. PROKA, 76344 Eggenstein-Leopoldshafen, Germany (fax +49−7247−808−666; E-mail: crysdata@fiz-karlsruhe.de) on quoting the depository numbers CSD-421383 (**1**) and CSD-421384 (**2**).

■ AUTHOR INFORMATION

Corresponding Author

*Phone: +46-8-16 21 69. Fax: +46-8-15 21 87. E-mail: mats.johnsson@mmk.su.se.

■ ACKNOWLEDGMENTS

M.J. and D.Z. thank the Swedish Research Council and the scientific program Highly Frustrated Magnetism supported by the European Science Foundation (ESF), P.L. thanks the German Science Foundation (DFG) and the NTH school "Contacs in Nanosystems", K.-W.C. thanks EuroMagNET II under the EC Contract 228043 and the Korean National Research Foundation (NRF) (2009-0093817). H.B. acknowledges financial support from the Swiss NSF and the NCCR MaNEP. M.-H.W. and J.L. thank the Office of Basic Energy Sciences, Division of Materials Sciences, U.S. Department of Energy for Grant DE-FG02-86ER45259 and the computing resources of the NERSC center and the HPC center of NCSU.

■ REFERENCES

(1) Johnsson, M.; Törnroos, K. W.; Mila, F.; Millet, P. *Chem. Mater.* **2000**, *12*, 2853−2857.
(2) Johnsson, M.; Törnroos, K. W.; Lemmens, P.; Millet, P. *Chem. Mater.* **2003**, *15*, 68−73.
(3) Becker, R.; Johnsson, M.; Kremer, R. K.; Klauss, H.-H.; Lemmens, P. *J. Am. Chem. Soc.* **2006**, *128*, 15469−15475.

(4) Takagi, R.; Johnsson, M.; Gnezdilov, V.; Kremer, R. K.; Brenig, W.; Lemmens, P. *Phys. Rev.* **2006**, *B74*, 014413.
(5) Jiang, H.-L.; Mao, J.-G. *Inorg. Chem.* **2006**, *45*, 7593−7599.
(6) Zhang, D.; Berger, H.; Kremer, R. K.; Wulferding, D.; Lemmens, P.; Johnsson, M. *Inorg. Chem.* **2010**, *49*, 9683−9688.
(7) Sidgwick, N. V.; Powell, H. M. *Proc. R. Soc. (London)* **1940**, *A176*, 153−180.
(8) Gillespie, R. J.; Nyholm, R. S. *Quart. Rev. London* **1957**, *11*, 339−380.
(9) Orgel, L. E. *J. Chem. Soc.* **1959**, *4*, 3815−3819.
(10) Seshadri, R.; Hill, N. A. *Chem. Mater.* **2001**, *13*, 2892−2899.
(11) Ok, K. M.; Halasyamani, P. S. *Inorg. Chem.* **2002**, *41*, 3805−3807.
(12) Waghmare, U. V.; Spaldin, N. A.; Kandpal, H. C.; Seshadri, R. *Phys. Rev. B* **2003**, *67*, 125111.
(13) Ok, K. M.; Halasyamani, P. S. *Angew. Chem., Int. Ed.* **2004**, *43*, 5489−5491.
(14) Stoltzfus, W.; Woodward, P. M.; Seshadri, R.; Klepeis, J.-H.; Bursten, B. *Inorg. Chem.* **2007**, *46*, 3839−3850.
(15) Becker, R.; Johnsson, M. *J. Solid State Chem.* **2007**, *180*, 1750−1758.
(16) Zhang, D.; Johnsson, M.; Berger, H.; Kremer, R. K.; Wulferding, D.; Lemmens, P. *Inorg. Chem.* **2009**, *48*, 6599−6603.
(17) *CrysAlisCCD and CrysAlisRED*; Oxford Diffraction Ltd.: Abingdon, Oxfordshire, England, 2006.
(18) Sheldrick, G. M. *Acta Crystallogr.* **2008**, *A64*, 112−122.
(19) Bergerhoff, G. *DIAMOND*; University of Bonn: Bonn, Germany, 1996.
(20) (a) Kresse, G.; Hafner, J. *Phys. Rev. B* **1993**, *47*, 558. (b) Kresse, G.; Furthmüller, J. *Comput. Mater. Sci.* **1996**, *6*, 15. (c) Kresse, G.; Furthmüller, J. *Phys. Rev. B* **1996**, *54*, 11169.
(21) Perdew, J. P.; Burke, K.; Ernzerhof, M. *Phys. Rev. Lett.* **1996**, *77*, 3865.
(22) Brown, I. D.; Altermatt, D. *Acta Crystallogr.* **1985**, *B41*, 244−247.
(23) Brese, N. E.; O'Keeffe, M. *Acta Crystallogr.* **1991**, *B47*, 192−197.
(24) Lueken, H. *Magnetochemie*; Teubner: Leipzig, Germany, 1999.
(25) Selwood, P. W. *Magnetochemistry*, 2nd ed.; Interscience: New York, 1956.
(26) Lemmens, P.; Eisener, B.; Brinkmann, M.; Gasparov, L. V.; Güntherodt, G.; Dongen, P. V.; Richter, W.; Steglich, F. *Phys. B (Amsterdam, Neth.)* **1996**, *223−224*, 535−537.
(27) Jensen, J.; Lemmens, P.; Gros, C. *Europhys. Lett.* **2003**, *64*, 689−695.
(28) Grove, M.; Lemmens, P.; Güntherodt, G.; Sales, B. C.; Büllesfeld, F.; Assmus, W. *Phys. Rev. B* **2000**, *61*, 6126−6132.
(29) Becker, R.; Johnsson, M.; Kremer, R.; Lemmens, P. *J. Solid State Chem.* **2005**, *178*, 2024−2029.
(30) Lemmens, P.; Güntherodt, G.; Gros, C. *Phys. Rep.* **2003**, *375*, 1−103.
(31) (a) Aroyo, M. I.; Perez-Mato, J. M.; Capillas, C.; Kroumova, E.; Ivantchev, S.; Madariaga, G.; Kirov, A.; Wondratschek, H. *Z. Kristallogr.* **2006**, *221*, 15−27. (b) Aroyo, M. I.; Kirov, A.; Capillas, C.; Perez-Mato, J. M.; Wondratschek, H. *Acta Crystallogr.* **2006**, *A62*, 115−128.
(32) (a) Choi, K. Y.; Lemmens, P.; Güntherodt, G.; Pashkevich, Yu. G.; Gnezdilov, V. P.; Reutler, P.; Pinsard-Gaudart, L.; Büchner, B.; Revcolevschi, A. *Phys. Rev.* **2005**, *B72*, 024301. (b) Choi, K. Y.; Lemmens, P.; Güntherodt, G.; Pashkevich, Yu. G.; Gnezdilov, V. P.; Reutler, P.; Pinsard-Gaudart, L.; Büchner, B.; Revcolevschi, V. *Phys. Rev.* **2005**, *B71*, 174402.
(33) Dudarev, S. L.; Botton, G. A.; Savrasov, S. Y.; Humphreys, C. J.; Sutton, A. P. *Phys. Rev. B* **1998**, *57*, 1505.
(34) Mayerová, Z.; Johnsson, M.; Lidin, S. *J. Solid State Chem.* **2005**, *178*, 3471−3475.